Observation of two-level critical-state in the van-der-Waals superconductor $Pt(Bi_{1-x}Se_x)_2$

Y. Samukawa,[1] M. Maeda,[1] N. Jiang,[1,2,3,*] R. Nakamura,[1] M. Watanabe,[1] K. Takaki,[1] Y. Moriyasu,[1] T. Ikushima,[1] T. Kida,[4] M. Hagiwara,[4] T. Nakamura,[5] Y. Okada,[5] K. Kudo,[1,3] and Y. Niimi[1,2,3]

[1]*Department of Physics, Graduate School of Science, Osaka University, Toyonaka 560-0043, Japan*
[2]*Center for Spintronics Research Network, Osaka University, Toyonaka 560-8531, Japan*
[3]*Institute for Open and Transdisciplinary Research Initiatives, Osaka University, Suita 565-0871, Japan*
[4]*Center for Advanced High Magnetic Field Science, Graduate School of Science, Osaka University, Toyonaka, Osaka 560-0043, Japan*
[5]*Okinawa Institute of Science and Technology Graduate University, Okinawa 904-0495, Japan*

(Received 6 March 2024; accepted 22 January 2025; published 7 February 2025)

Trigonal $PtBi_2$ is one of the attractive van-der-Waals materials because of the enhancement of its superconducting transition temperature T_c by doping chalcogen elements such as Se and Te. Recently, it has been reported that T_c of $Pt(Bi_{1-x}Se_x)_2$ is enhanced by a factor of four, compared to the pristine $PtBi_2$, together with the polar-nonpolar structural phase transition. Thus, it is desirable to study electrical transport properties of this new superconducting compound. Here, we have performed magnetotransport measurements on $Pt(Bi_{1-x}Se_x)_2$ ($x = 0.06$ and 0.08) thin-film devices and observed a peculiar magnetoresistance, where a finite hysteresis appears when the superconducting state is broken. By measuring the magnetoresistance systematically, we have attributed this behavior to the two-level critical state where fluxons pinned in $Pt(Bi_{1-x}Se_x)_2$ play an important role.

DOI: 10.1103/PhysRevB.111.064506

I. INTRODUCTION

In recent years, van-der-Waals (vdW) materials have attracted much attention from the viewpoints of the low-dimensional physics as well as of the next-generation electronic devices owing to easy processing into thin-film forms. Amongst a wide variety of vdW materials, ultrathin transition metal dichalcogenides such as MoS_2 [1–4], $NbSe_2$ [5–7], TaS_2 [8–11], and WTe_2 [12,13] are being studied extensively from the perspective of two-dimensional superconductivity. In order to expand the material groups of thin-film superconductors, it is important to explore other vdW superconductors.

Trigonal $PtBi_2$ is an attractive noncentrosymmetric vdW material with a space group of $P31m$ [see Fig. 1(a)] [14]. It has fascinating properties such as huge linear magnetoresistance because of the band structure [15,16], large Rashba splitting [17], superconductivity at the transition temperature $T_c = 0.6$ K [18], pressure-induced superconductivity [19], and triple point near the Fermi surface [20]. By doping Se into the Bi site, the polar-nonpolar structural phase transition takes place at the doping rate x of 3.2%, showing the centrosymmetric crystal structure with a space group $P\bar{3}m1$ [see Fig. 1(b)] [21]. Along with the structural transition, T_c increases from 0.6 K to 2.4 K. After this critical doping rate, T_c monotonically decreases. Although the microscopic origin of the enhancement of T_c is not clear, $Pt(Bi_{1-x}Se_x)_2$ is a new type of vdW superconductor in which T_c increases with structural phase transition.

In this paper, we have studied electrical transport properties in superconducting $Pt(Bi_{1-x}Se_x)_2$ thin-film devices with $x = 0.06$ and 0.08. A clear hysteresis in magnetoresistance was observed near the critical magnetic field $\mu_0 H_{c2}$, where μ_0 is the permeability in vacuum. This hysteresis has the opposite sign to the conventional hysteresis: in other words, the superconductivity is broken with a small applied magnetic field in comparison to the applied field when the superconductivity is recovered. By measuring $\mu_0 H_{c2}$ not only as a function of temperature but also as a function of magnetic-field sweep rate and maximum applied field, we have attributed this hysteresis to the two-level critical-state caused by inhomogeneities of the superconducting state [22].

II. EXPERIMENTAL METHODS

Single crystalline samples of $Pt(Bi_{1-x}Se_x)_2$ were synthesized by using the same method as a previous study reported by some of the present authors [21]. A stoichiometric mixture of Pt (99.95%), Bi (99.99%), and Se (99.9%) powders was sealed in an evacuated quartz tube and heated at 630°C for 24 hours, followed by quenching in ice water. The chemical compositions of the obtained samples were estimated by energy dispersive x-ray spectroscopy (EDS) using a TM4000Plus II scanning electron microscope (Hitachi High-Tech) equipped with an AztecOne energy dispersive spectrometer (Oxford Instruments) under the conditions of an accelerating voltage of 15 kV and currents of 0.8–1 nA. The crystal structure was examined by powder x-ray diffraction (XRD) using a MiniFlex600-C x-ray diffractometer equipped with a D/teX Ultra2-high-speed one-dimensional detector (Rigaku). We obtained thin flakes through the mechanical exfoliation technique using scotch tapes.

The flakes were transferred onto Si/SiO_2 substrates, and the electrodes were patterned by electron beam lithography,

*Contact author: nan.jiang@phys.sci.osaka-u.ac.jp

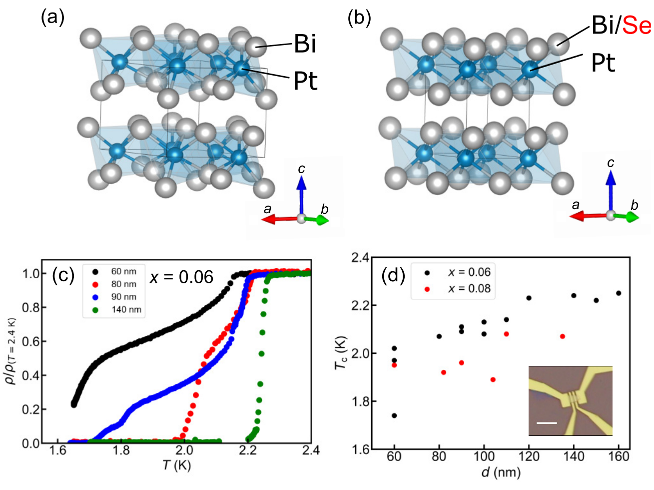

FIG. 1. [(a), (b)] Crystal structures of $PtBi_2$ with a space group of $P31m$ and $Pt(Bi_{1-x}Se_x)_2$ with a space group of $P\bar{3}m1$, respectively. (c) Temperature dependence of electrical resistivity ρ near T_c for $x = 0.06$ with different thicknesses, 60 nm (black dots), 80 nm (red dots), 90 nm (blue dots), and 140 nm (green dots). The vertical axis is normalized by ρ at $T = 2.4$ K. (d) Thickness d dependence of T_c for $x = 0.06$ (black dots) and $x = 0.08$ (red dots) devices. The inset is an optical microscope image of a typical device. The white bar in the inset corresponds to 5 μm.

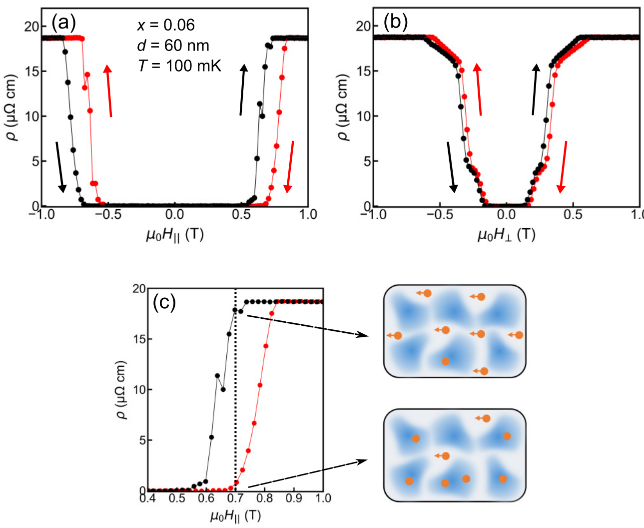

FIG. 2. Magnetic field dependence of ρ under (a) the in-plane and (b) out-of-plane magnetic fields measured with a device of $x = 0.06$ and $d = 60$ nm at 100 mK. The magnetic-field sweep rate is 0.065 T/min and the applied maximum field is 2 T. Black and red dots represent data from −2 T to 2 T and data from 2 T to −2 T, respectively. We only show the magnetic field range in between −1 T and 1 T to focus on the hysteresis behavior. (c) Closeup view of (a), together with schematic images of fluxons trapped inside the device based on the two-level critical-state model. The blue and gray areas in the schematic images represent strong and weak superconductivity regions, respectively. The orange dots represent fluxons in the superconductivity region. The fluxons in the weak superconductivity region can move by the electric current and generate a voltage, while the fluxons in the strong superconductivity region cannot move by the strong pinning potential, resulting in zero resistivity.

followed by depositing Ti/Au films. An optical microscope image of our typical device is shown in the inset of Fig. 1(d). The thickness d of each flake was measured by an atomic force microscope (NanoNaviReal Probe Station). The devices were cooled using a dilution refrigerator (Oxford Instruments) with a superconducting magnet or a ^{4}He flow refrigerator with an electromagnet, depending on the temperature range to be measured. The measurements of electrical transport properties were performed by the conventional four terminal method through a lock-in amplifier (SR-830).

Additionally, we performed scanning tunneling microscope (STM) measurements to investigate the inhomogeneity of Se doping. STM experiments were performed using an electrochemically etched W tip, which was annealed in ultrahigh vacuum (UHV) and conditioned on a Au(111) surface. Single crystals of $Pt(Bi_{1-x}Se_x)_2$ were cleaved in UHV at room temperature and immediately transferred to the STM head, maintained at 4.2 K, following cleavage.

III. RESULTS AND DISCUSSIONS

In Fig. 1(c), we show the temperature dependence of electrical resistivity ρ normalized by the resistivity at 2.4 K, $\rho(T = 2.4\,\mathrm{K})$, for $x = 0.06$ devices with several different thicknesses. The resistivity starts to drop at around 2.2 K, reflecting the onset of the superconductivity phase transition. The temperature where ρ reaches zero is lower for thinner devices. To characterize such a tendency, we plot the d dependence of T_c, defined by half the resistivity of the normal state, for $x = 0.06$ and 0.08 in Fig. 1(d). All the raw data shown in Fig. 1(d) are presented in Fig. 7 in Appendix A. T_c decreases with decreasing d for both Se concentrations. This tendency is consistent with other thin-film superconductors [23–26].

This d dependence of T_c can be explained by the inhomogeneity in the superconducting state. In $Pt(Bi_{1-x}Se_x)_2$, the superconductivity should be nonuniform. In other words, there should be strong (or weak) superconducting regions. Such inhomogeneity should be induced by spatially nonuniform doping of Se and spatially nonuniform strain. When d approaches the characteristic inhomogeneity length, T_c would be reduced as discussed in a previous study [27]. The inhomogeneity of the superconductivity also leads to the broadening of the superconducting transition in the ρ versus T curve in Fig. 1(c). We will discuss this inhomogeneity in the last part of this section.

Next, we discuss magnetotransport properties of $Pt(Bi_{1-x}Se_x)_2$ thin-film devices. In Figs. 2(a) and 2(b), we show the in-plane magnetic field $\mu_0H_{||}$ and out-of-plane magnetic field $\mu_0H_{\perp}$ dependencies of ρ at 100 mK measured with a device of $x = 0.06$ and $d = 60$ nm. We have observed a hysteresis near μ_0H_{c2} in both cases. We note that the observed hysteresis is opposite to the well-known hysteresis, which typically retains the characteristics of the previous state. When the magnetic field is swept from zero to a large value (positive sweep), μ_0H_{c2} is smaller compared to the case when the magnetic field is swept from a large value to zero (negative sweep) in our devices as shown in Figs. 2(a) and 2(b), while μ_0H_{c2} of the positive sweep is larger than that of the negative sweep in the conventional hysteresis. We also observed the similar hysteresis with the bulk sample (not shown here). The magnitude of the hysteresis is larger for the in-plane configuration compared to the out-of-plane configuration.

The similar hysteresis has often been observed in inhomogeneous superconducting materials such as granular cuprate superconductors [28–32], and can be explained by the two-level critical-state model [22]. In this model, there are two regions, i.e., weak and strong superconducting regions, corresponding to the gray and blue areas in Fig. 2(c), respectively. By applying the magnetic field more than the lower critical field in the positive sweep, fluxons are induced mainly in the weak superconducting region. The fluxons that penetrate into the weak superconducting region can freely move with a small bias current, resulting in nonzero resistivity at this magnetic field. As the magnetic field is further increased, the fluxons penetrate also into the strong superconducting region and eventually the resistivity returns to the normal state. We then decrease the magnetic field from the large value. The fluxons start to escape from the weak superconducting region because of the weaker pinning potential compared to the strong superconducting region. As a result, even at the same external magnetic field, there are more fluxons left in the strong superconducting region in the negative sweep. The fluxons trapped in the strong pinning potential cannot move in the sample. This results in a lower resistivity, that is, a higher $\mu_0 H_{c2}$ [$\mu_0 H_r$ in Fig. 3(a)] in the negative sweep, as schematically illustrated in Fig. 2(c).

In $Pt(Bi_{1-x}Se_x)_2$ thin-film devices, owing to the spatially nonuniform Se doping and strain, there should be different regions of different pinning strength with a size of several tens nanometers when it becomes superconducting. As already discussed in Fig. 1(c), the fact that the superconducting transition becomes broader with decreasing d is supportive to apply the two-level critical-state model to our experimental results. We will discuss the origin of the two regions, i.e., weak and strong superconducting regions, in the last part of this section.

To ensure the applicability of the two-level critical-state model to our $Pt(Bi_{1-x}Se_x)_2$ thin-film devices, we changed several parameters such as the magnetic-field sweep rate, the maximum magnetic field, and the temperature, to measure the hysteresis. Since the magnitude of the hysteresis is larger in the in-plane configuration as shown in Figs. 2(a) and 2(b), we mainly focus on the magnetoresistance under $\mu_0 H_{||}$ in the following analysis. In Appendix B, we also discuss the magnetic-field sweep rate dependence of the magnetoresistance under $\mu_0 H_{\perp}$. In order to quantitatively evaluate the magnitude of the hysteresis in the ρ versus $\mu_0 H_{||}$ curves, we have defined the difference between $\mu_0 H_r$ and $\mu_0 H_c$ as $\Delta\mu_0 H_{c2}(\equiv \mu_0 H_r - \mu_0 H_c)$, where $\mu_0 H_r$ and $\mu_0 H_c$ are the magnetic fields at which ρ takes half of the resistivity in the normal state during the negative and positive sweeps, respectively [see Fig. 3(a)].

We first changed the magnetic-field sweep rate, keeping other parameters unchanged. Because of the specification of our current supply, we need to stop the sweeping of magnetic field when taking the resistivity data. Therefore, the magnetic-field sweep rate is defined as the averaged value during the measurement. As shown in Fig. 3(b), $\mu_0 H_r$ is almost independent of the magnetic-field sweep rate, while

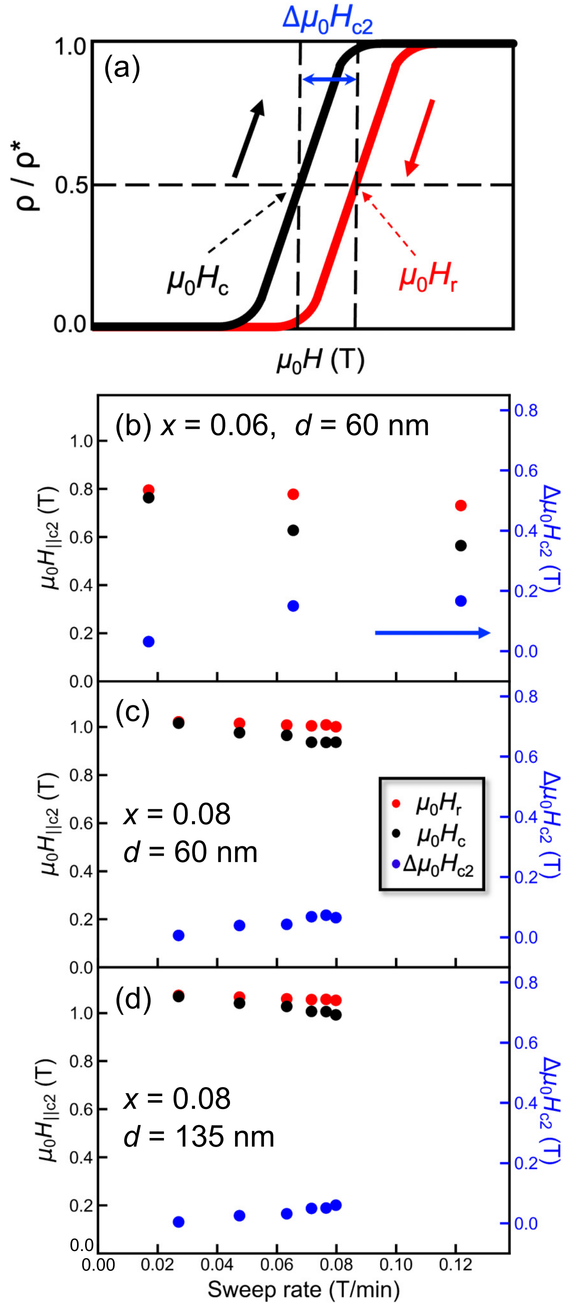

FIG. 3. (a) A schematic illustration of the hysteresis behavior to define each parameter. The vertical axis is normalized by ρ at $\mu_0 H = 1.2$ T ($\equiv \rho^*$). $\mu_0 H_r$ and $\mu_0 H_c$ are defined as the magnetic fields at which ρ becomes half of the resistivity in the normal state during the negative and positive sweeps, respectively. The magnitude of the hysteresis is defined as $\Delta\mu_0 H_{c2} \equiv \mu_0 H_r - \mu_0 H_c$. (b)–(d) The magnetic-field sweep rate dependence of $\mu_0 H_r$ (red dots), $\mu_0 H_c$ (black dots), and $\Delta\mu_0 H_{c2}$ (blue dots) measured at $T = 100$ mK with devices of (b) $x = 0.06$ and $d = 60$ nm, (c) $x = 0.08$ and $d = 60$ nm, and (d) $x = 0.08$ and $d = 135$ nm. The maximum magnetic field of ± 2 T was applied along the in-plane direction of the devices.

$\mu_0 H_c$ decreases as increasing the magnetic-field sweep rate. This results in an increase of $\Delta\mu_0 H_{c2}$ with increasing the sweep rate. The same tendency has been confirmed for multiple devices with the other concentration $x = 0.08$ and other thicknesses [see Figs. 3(c) and 3(d)]. All the raw data shown in Fig. 3 are presented in Fig. 8 in Appendix A. The above behavior can be understood within the framework of the two-level critical-state model. As explained in Fig. 2(c), fluxons are first induced in the weak superconducting region as the magnetic field is increased. The induced fluxons move due to a bias electric current and/or thermal fluctuation. In such a process, some fluxons may go into the strong superconducting region and become trapped by a strong pinning potential. If the magnetic-field sweep rate is extremely slow, most of the fluxons are trapped in the strong superconducting region resulting in a lower resistivity and thus higher $\mu_0 H_c$. This is more noticeable in the positive sweep because there are more fluxons in the weak superconductivity region, compared to the negative sweep. As a result, $\mu_0 H_c$ increases with decreasing the magnetic-filed sweep rate, while $\mu_0 H_r$ is almost independent of the magnetic-field sweep rate, leading to the reduction of $\Delta\mu_0 H_{c2}$.

We next changed the maximum magnetic field, keeping the magnetic-field sweep rate constant (0.065 T/min for $x = 0.06$ device and 0.077 T/min for $x = 0.08$ devices). In Figs. 4(a)–4(c), we show the maximum in-plane magnetic filed $\mu_0 H_{||\max}$ dependence of $\mu_0 H_r$ and $\mu_0 H_c$ measured with the same devices as in Figs. 3(b)–3(d). $\mu_0 H_r$ gradually increases with increasing $\mu_0 H_{||\max}$ and is saturated above 2 T, while $\mu_0 H_c$ dose not show a noticeable field dependence. The variation for $\mu_0 H_c$ stems from the resistivity jump owing to sudden flux changes inside the superconductor, which is also discussed in the previous paper [33]. To compare $\mu_0 H_r$ obtained with different devices, we plot $\mu_0 H_r$ normalized by the value of $\mu_0 H_r$ at $\mu_0 H_{||\max} = 2$ T ($\equiv \mu_0 H^*$). For all the investigated devices, it shows the same tendency as explained above. The $\mu_0 H_{||\max}$ dependence of $\mu_0 H_r$ can also be understood by the two-level critical-state model. Considering the negative sweep process, the system shows zero resistivity when there is almost no fluxon in the weak superconducting region [see the bottom schematic in Fig. 2(c)]. In this situation, the external magnetic field is nearly equal to the summation of fluxons trapped in the strong superconducting region. Thus, the magnitude of $\mu_0 H_r$ is proportional to the number of fluxons pinned in the strong superconducting region. Even after ρ gets back to the same value as in the normal state under a magnetic field, not all the pinning sites in the strong superconducting region are fully occupied when $\mu_0 H_{||\max}$ is not sufficiently large. In other words, there is some room to trap fluxons in the strong superconducting region. With increasing $\mu_0 H_{||\max}$, we can pin more fluxons in the strong superconducting region. As a result, $\mu_0 H_r$ continuously increases until all the pinning sites in the strong superconducting region are occupied, and is eventually saturated. This scenario not only supports the two-level critical-state model but also indicates that the pinning sites are fully occupied at around 2 T in our $Pt(Bi_{1-x}Se_x)_2$ thin-film devices. The similar maximum magnetic field dependence of $\mu_0 H_r$ was also reported in granular cuprate superconductors [31] and oxygen-annealed FeTe thin-films [34] where all the results were also well explained by the two-level critical-state model. Furthermore, there are multisteps in the I-V curves as shown in Fig. 10 in Appendix C, which is indicative of the presence of superconducting regions with different strengths.

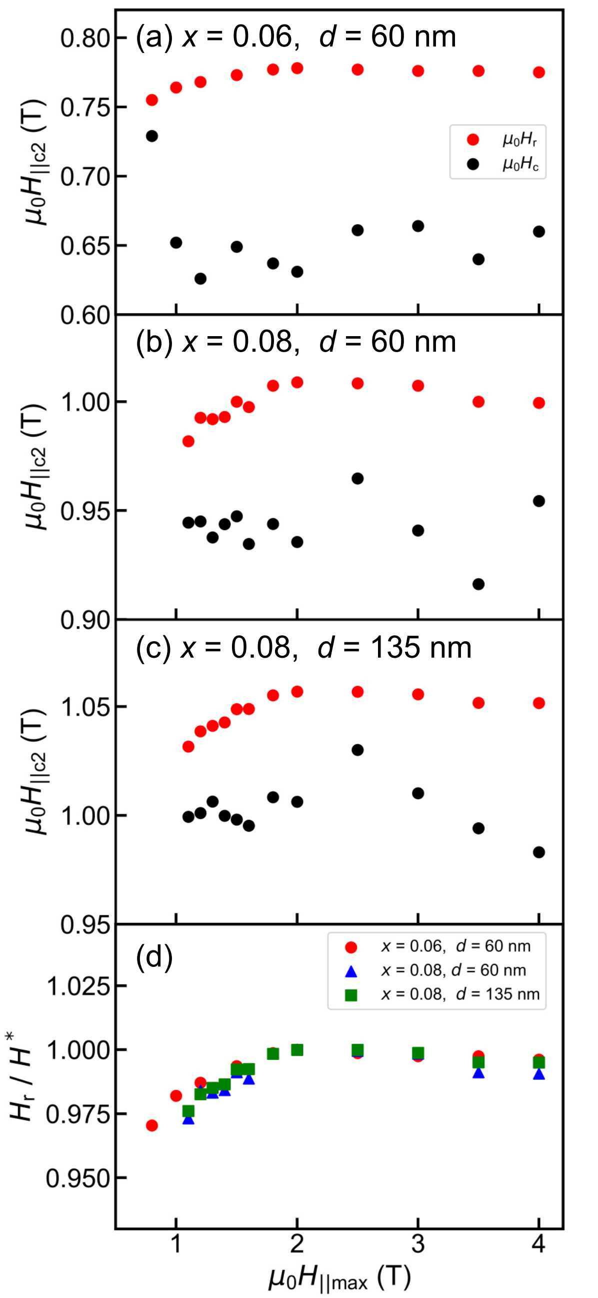

FIG. 4. (a)–(c) The maximum in-plane magnetic field $\mu_0 H_{||\max}$ dependence of $\mu_0 H_r$ (red dots) and $\mu_0 H_c$ (black dots) measured at $T = 100$ mK using the same devices as in Figs. 3(b)–3(d). The magnetic-field sweep rate is 0.065 T/min for (a), and 0.077 T/min for (b) and (c). (d) The $\mu_0 H_{||\max}$ dependence of $\mu_0 H_r$ normalized by $\mu_0 H^*$, which is the $\mu_0 H_r$ value at $\mu_0 H_{||\max} = 2$ T, obtained with the same devices as in Figs. 3(b)–3(d): $x = 0.06$ and $d = 60$ nm (red circles), $x = 0.08$ and $d = 60$ nm (blue triangles), and $x = 0.08$ and $d = 135$ nm (green rectangles).

In Fig. 5, we show the temperature dependence of $\mu_0 H_r$ and $\mu_0 H_c$ measured with the same devices as in Figs. 3 and 4 under the magnetic-field sweep rate of 0.065 T/min for Figs. 5(a) and 5(b) and 0.077 T/min for Figs. 5(c) and 5(d). The maximum field $\mu_0 H_{\max}$ has been fixed to 2 T. With increasing temperature, $\mu_0 H_r$ and $\mu_0 H_c$ monotonically decrease

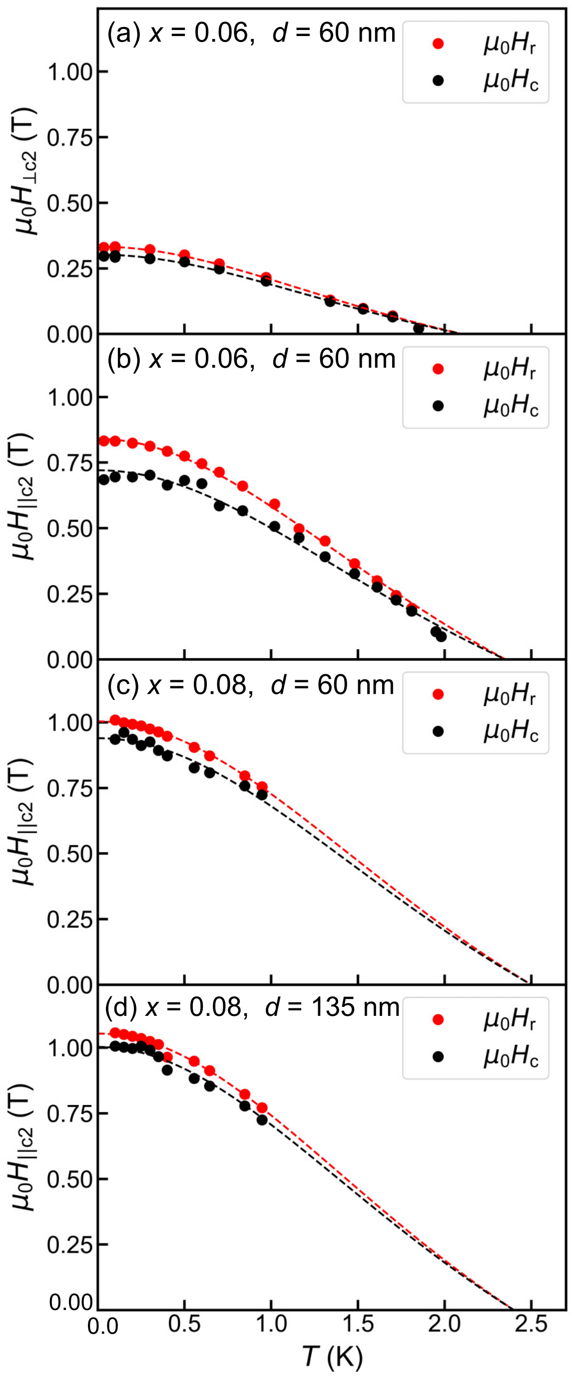

FIG. 5. Temperature dependence of $\mu_0 H_\mathrm{r}$ (red circles) and $\mu_0 H_\mathrm{c}$ (black circles) under (a) the out-of-plane and (b) in-plane magnetic fields measured with the same device as in Fig. 3(b). [(c), (d)] Temperature dependence of $\mu_0 H_\mathrm{r}$ and $\mu_0 H_\mathrm{c}$ under the in-plane magnetic field using the same devices as in Figs. 3(c) and 3(d), respectively. The magnetic-field sweep rates of 0.065 T/min for (a) and (b), and 0.077 T/min for (c) and (d). The maximum filed $\mu_0 H_\mathrm{max}$ is fixed to 2 T. The dotted lines are the best fits with the Ginzburg-Landau formula, $\mu_0 H_{c2}(\mathrm{T}) = \mu_0 H_{c2}(0)\frac{1-(\frac{T}{T_c})^2}{1+(\frac{T}{T_c})^2}$ [35].

toward T_c, indicating that $\Delta\mu_0 H_{c2}$ becomes zero at T_c. This temperature dependence clearly demonstrates that the observed hysteresis comes from the superconducting properties. The result also supports that the hysteresis is well explained by the two-level critical-state model. The similar behavior was also reported in FeTe thin films where the two-level critical-state model was used to explain the results [34].

Lastly, we discuss the origin of the two-level critical state. As already mentioned, a similar hysteresis described by the two-level critical-state model was reported in granular cuprate superconductors [28–32], Bi nanowire [36], FeTe thin-films annealed in oxygen atmosphere [34], and Bi/Ni bilayer [33].

T_c of $\mathrm{Pt(Bi_{1-x}Se_x)_2}$ ($\approx$2 K $\approx$ 0.17 meV) is much lower than those of FeTe ($\approx$10 K $\approx$ 0.9 meV) and cuprates ($\approx$90 K $\approx$ 7.8 meV) where the two-level critical-state model is applicable, and its H_{c2} is also smaller. On the other hand, T_c and H_{c2} of $\mathrm{Pt(Bi_{1-x}Se_x)_2}$ are comparable to those of Bi nanowires ($T_\mathrm{c} \approx 0.6$ K ≈ 0.05 meV) and Bi/Ni bilayers ($T_\mathrm{c} \approx 1.5$ K ≈ 0.13 meV). The hysteresis observed in these systems, which has been attributed to the two-level critical-state model, is of the same order as that observed in our results. This similarity is supportive for our two-level critical-state model scenario for $\mathrm{Pt(Bi_{1-x}Se_x)_2}$.

In these cases, the origin of the two-level critical state can be attributed to the granular nature of the amount of oxygen [28–32] for cuprate superconductors, the inhomogeneity of oxidized region in FeTe films [34], the spatial thickness fluctuation of ferromagnetic thin film in Bi/Ni bilayer [33].

In our $\mathrm{Pt(Bi_{1-x}Se_x)_2}$ thin-film devices, the inhomogeneity of superconductivity could be induced by the two possible reasons: one is caused by spatially nonuniform doping of Se and the other is spatially nonuniform strain. As explained in the introduction, T_c monotonically decreases as the amount of Se doping is increased after the structural phase transition [21]. This means that the superconductivity is weaker in Se-rich regions, and thus spatially nonuniform doping of Se results in a nonuniform distribution of regions with different superconducting strengths. From the EDS data, no inhomogeneity of Se doping is observed, indicating that the Se doping is uniform on the scale of the EDS spot size, which is typically on the order of a few micrometers, as shown in Fig. 6(a). To investigate the inhomogeneity of Se doping on a smaller scale, we conducted STM measurements. Figure 6(b) shows a constant-current topographic image of $\mathrm{Pt(Bi_{1-x}Se_x)_2}$ with $x = 0.08$ at 4 K. Several levels of contrast are observed compared to the topographic image of trigonal $\mathrm{PtBi_2}$ [37], which may correspond to different electronic states possibly arising from Se doping. Considering that the coherence length of $\mathrm{Pt(Bi_{1-x}Se_x)_2}$ is on the order of several tens of nanometers, we have included Gaussian broadening with a full width at half maximum (FWHM) of 60 nm into the STM image, as shown in Fig. 6(c). This image suggests the presence of inhomogeneity in the electronic states on the scale of the coherence length. Although scanning tunneling spectroscopy well below T_c is required to accurately determine the inhomogeneity of superconducting strength, Fig. 6(c) is supportive for our two-level critical-state model scenario and consistent with the assumption discussed in Fig. 2(c).

In addition, a strain can also modulate the superconductivity strength [19]. As explained in Sec. II, quenching in ice water was performed to obtain $\mathrm{Pt(Bi_{1-x}Se_x)_2}$ bulk samples. In this process, a spatially nonuniform strain would be introduced because such a rapid temperature change induces spatially nonuniform thermal contraction. This type of strain

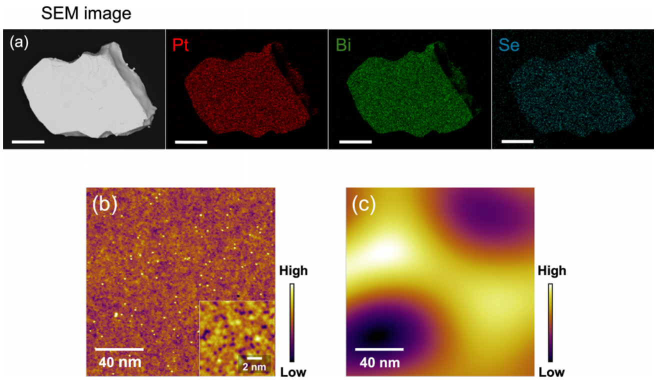

FIG. 6. (a) Scanning electron microscope (SEM) image and EDS elemental maps of $Pt(Bi_{1-x}Se_x)_2$ with $x = 0.08$. Each represents the elemental mapping of Pt(red), Bi(green), and Se(cyan). The white bars correspond to 100 µm. (b) Constant-current topographic image of $Pt(Bi_{1-x}Se_x)_2$ with $x = 0.08$ at 4 K. The feedback conditions are –300 mV and 50 pA. The inset shows a magnified view of the main image, with feedback conditions of –20 mV and 2.0 nA. (c) Topographic image with Gaussian broadening applied, with a full width at half maximum (FWHM) of 60 nm.

induced by high-rate thermal-cycles was also discussed in $PtSe_2$ [38]. Replacement of the Bi sites by Se can also cause local strain because Se has a smaller atomic radius than Bi. At the moment, however, we cannot conclude which mechanism is more dominant for the present results. Thus, further experiments, such as scanning tunneling spectroscopy well below T_c and the exploration of various doping materials, are needed to elucidate the origin of the two-level critical-state.

IV. CONCLUSIONS

In conclusion, we have measured magnetotransport properties in a vdW superconductor $Pt(Bi_{1-x}Se_x)_2$. A clear hysteresis behavior was observed in the magnetic field dependence of the resistivity. This hysteresis has the opposite sign to the conventional one. In order to identify the origin of the hysteresis, we varied the magnetic-field sweep rate, the maximum magnetic field, and the temperature when the resistivity was measured as a function of the magnetic field. Through these measurements, we have attributed the origin of such a hysteresis to the two-level critical-state model. The present results demonstrate the importance of the two-level critical-state in vdW superconductors and suggest a new analytical tool for superconducting compounds with large inhomogeneities.

ACKNOWLEDGMENTS

This work was supported by JSPS KAKENHI (Grants No. JP20H02557, No. JP21J20477, No. JP22H04481, No. JP23H00257, No. JP23K13062, No. JP19H05823, No. JP22H01182, No. JP23K22453, and No. JP24K21531) and JST FOREST (Grant No. JPMJFR2134). Part of the characterization of the bulk samples was performed at the Center for Advanced High Magnetic Field Science in Osaka University under the Visiting Researcher's Program of the Institute for Solid State Physics, the University of Tokyo, and at Analytical Instrument Facility, Graduate School of Science, Osaka University, using research equipment shared under the MEXT Project for promoting public utilization of advanced research infrastructure (JPMXS0441200023).

APPENDIX A: TEMPERATURE AND MAGNETIC FIELD DEPENDENCE OF RESISTIVITY

In Fig. 7, we present the raw data of the temperature dependence of ρ for films with different thicknesses to obtain T_c, as shown in Fig. 1(d): (a) $x = 0.06$ and (b) $x = 0.08$. As the thickness decreases, the superconducting transition becomes broader and exhibits multiple transitions, suggesting the presence of inhomogeneity in the superconducting state. This tendency is consistent with the thickness dependence of T_c, which is defined as the temperature at which the resistivity reaches half of the normal-state value, as shown in Fig. 1(d). These data support the validity of our analysis in Fig. 1(d).

Figure 8 are the raw data of Fig. 3. Figures 8(a)–8(c) show the magnetic field dependence of ρ at 100 mK for a device with $x = 0.06$ and $d = 60$ nm, measured at sweep rates of 0.017, 0.065, and 0.12 T/min, respectively. Figures 8(d)–8(f) display the magnetic field dependence of ρ at 100 mK for a device with $x = 0.08$ and $d = 60$ nm, measured at sweep rates of 0.027, 0.063, and 0.080 T/min, respectively. Figures 8(g)–8(i) show the magnetic field dependence of ρ at 100 mK for a device with $x = 0.08$ and $d = 135$ nm, measured at sweep rates of 0.027, 0.063, and 0.080 T/min, respectively. Although some jumps are observed during the positive sweep, the magnitude of the hysteresis increases as the sweep rate increases. These raw data support the validity

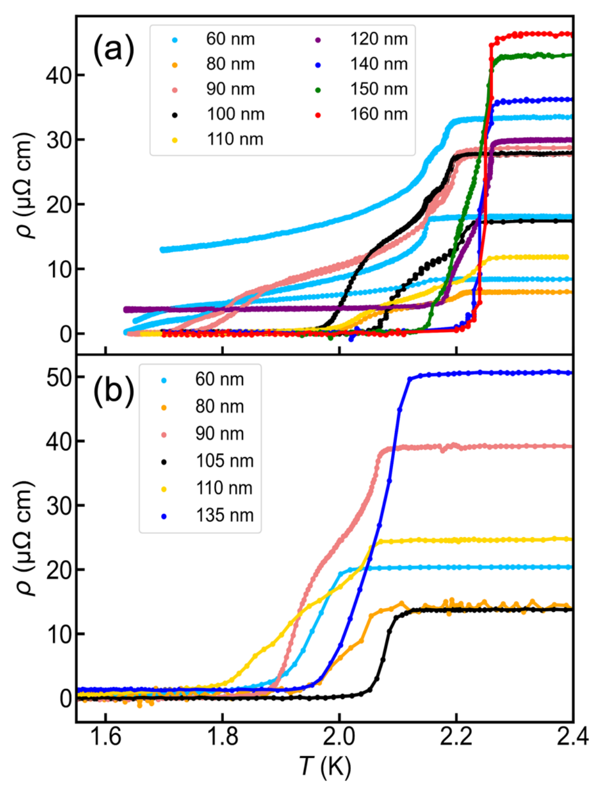

FIG. 7. The temperature dependence of resistivity for different film thicknesses to obtain T_c in Fig. 1 (d). (a) $x = 0.06$ and (b) $x = 0.08$.

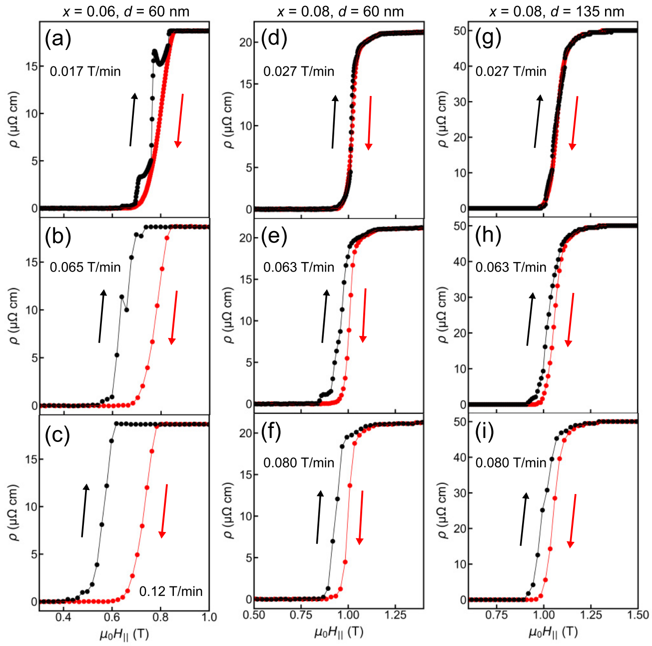

FIG. 8. (a)–(c) Raw data of Fig. 3(b) with the sweep rates of 0.017, 0.065, and 0.12 T/min, respectively. (d)–(f) Raw data of Fig. 3(c) with the sweep rates of 0.027, 0.063, and 0.080 T/min, respectively. (g)–(i) Raw data of Fig. 3(d) with the sweep rates of 0.027, 0.063, and 0.080 T/min, respectively.

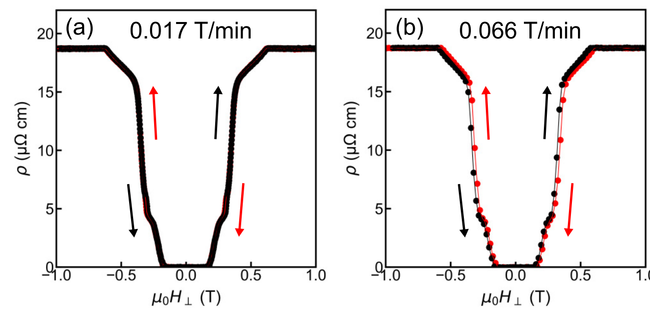

FIG. 9. Magnetic field dependence of ρ under the out-of-plane magnetic field with a device of $x = 0.06$, $d = 60$ nm at 100 mK, and $\mu_0 H_{\max}$ is fixed at 1 T. The magnetic-field sweep rate is 0.017 T/min for (a) and 0.066 T/min for (b). The magnetic-field sweep rate for (a) is slow enough so that the hysteresis is negligibly small.

of our method for evaluating the magnitude of the hysteresis as $\Delta\mu_0 H_{c2}$, demonstrating the suitability for investigating the sweep rate dependence of the hysteresis, as shown in Fig. 3.

APPENDIX B: SWEEP RATE DEPENDENCE OF THE HYSTERESIS UNDER OUT-OF-PLANE MAGNETIC FIELD

In the magnetic field dependence of resistivity, a distinct multistep transition is observed under an out-of-plane magnetic field, whereas the transition is smoother under an in-plane magnetic field, as shown in Fig. 2. This behavior is likely attributed to the difference in fluxon penetration between the out-of-plane and in-plane directions, which are influenced by the device geometry. In other words, the out-of-plane magnetic field is more sensitive for detecting inhomogeneities within the device. Furthermore, the observed multi-step transition suggests variations in superconducting strength within the single thin-film device, supporting our two-level critical-state model scenario in $Pt(Bi_{1-x}Se_x)_2$.

Despite the presence of three distinct regions in the magnetoresistance under an out-of-plane magnetic field, the hysteresis behavior is consistent with that observed under the in-plane magnetic field. In Fig. 9, we present the magnetoresistance under the out-of-plane magnetic field for different field sweep rates. Similar to the in-plane magnetic field results shown in Fig. 3, the hysteresis vanishes as the sweep rate decreases. However, the width of the hysteresis in the out-of-plane field is significantly smaller than that in the in-plane field.

APPENDIX C: I-V CHARACTERISTICS

Figure 10 shows the I-V characteristic of $Pt(Bi_{1-x}Se_x)_2$ with $x = 0.06$ and $d = 60$ nm, measured at $T = 40$ mK. As illustrated in Fig. 10(b), two distinct jumps corresponding to the critical currents are observed. This observation indicates the presence of superconducting regions with different strengths within $Pt(Bi_{1-x}Se_x)_2$, supporting the validity of the two-level critical-state model.

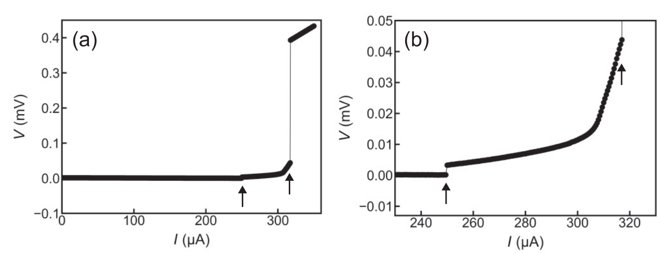

FIG. 10. $I - V$ characteristic of $x = 0.06$, $d = 60$ nm measured at $T = 40$ mK. (a) $I - V$ characteristic in the dc current range from 0 to 350 μA. (b) An enlarged view near the critical current region in (a). Two jumps are observed, supporting a two-level critical-state in our devices.

[1] J. T. Ye, Y. J. Zhang, R. Akashi, M. S. Bahramy, R. Arita, and Y. Iwasa, Superconducting dome in a gate-tuned band insulator, Science **338**, 1193 (2012).

[2] J. M. Lu, O. Zheliuk, I. Leermakers, N. F. Q. Yuan, U. Zeitler, K. T. Law, and J. T. Ye, Evidence for two-dimensional Ising superconductivity in gated MoS_2, Science **350**, 1353 (2015).

[3] Y. Saito, Y. Nakamura, M. S. Bahramy, Y. Kohama, J. Ye, Y. Kasahara, Y. Nakagawa, M. Onga, M. Tokunaga, T. Nojima, Y. Yanase, and Y. Iwasa, Superconductivity protected by spin–valley locking in ion-gated MoS_2, Nat. Phys. **12**, 144 (2016).

[4] D. Costanzo, S. Jo, H. Berger, and A. F. Morpurgo, Gate-induced superconductivity in atomically thin MoS_2 crystals, Nat. Nanotechnol. **11**, 339 (2016).

[5] X. Xi, Z. Wang, W. Zhao, J.-H. Park, K. T. Law, H. Berger, L. Forró, J. Shan, and K. F. Mak, Ising pairing in superconducting $NbSe_2$ atomic layers, Nat. Phys. **12**, 139 (2016).

[6] H. Wang, X. Huang, J. Lin, J. Cui, Y. Chen, C. Zhu, F. Liu, Q. Zeng, J. Zhou, P. Yu, X. Wang, H. He, S. H. Tsang, W. Gao, K. Suenaga, F. Ma, C. Yang, L. Lu, T. Yu, E. H T. Teo, High-quality monolayer superconductor $NbSe_2$ grown by chemical vapour deposition, Nat. Commun. **8**, 394 (2017).

[7] X. Xi, L. Zhao, Z. Wang, H. Berger, L. Forró, J. Shan, and K. F. Mak, Strongly enhanced charge-density-wave order in monolayer $NbSe_2$, Nat. Nanotechnol. **10**, 765 (2015).

[8] S. C. de la Barrera, M. R. Sinko, D. P. Gopalan, N. Sivadas, K. L. Seyler, K. Watanabe, T. Taniguchi, A. W. Tsen, X. Xu, D. Xiao, and B. M. Hunt, Tuning Ising superconductivity with layer and spin–orbit coupling in two-dimensional transition-metal dichalcogenides, Nat. Commun. **9**, 1427 (2018).

[9] Y. Yu, F. Yang, X. F. Lu, Y. J. Yan, Y.-H. Cho, L. Ma, X. Niu, S. Kim, Y.-W. Son, D. Feng, S. Li, S.-W. Cheong, X. H. Chen, and Y. Zhang, Gate-tunable phase transitions in thin flakes of 1T-TaS_2, Nat. Nanotechnol. **10**, 270 (2015).

[10] E. Navarro-Moratalla, J. O. Island, S. Mañas-Valero, E. Pinilla-Cienfuegos, A. Castellanos-Gomez, J. Quereda, G. Rubio-Bollinger, L. Chirolli, J. A. Silva-Guillén, N. Agraït, G. A. Steele, F. Guinea, H. S. J. van der Zant, and E. Coronado, Enhanced superconductivity in atomically thin TaS_2, Nat. Commun. **7**, 11043 (2016).

[11] J. Pan, C. Guo, C. Song, X. Lai, H. Li, W. Zhao, H. Zhang, G. Mu, K. Bu, T. Lin, X. Xie, M. Chen, and F. Huang, Enhanced superconductivity in restacked TaS_2 nanosheets, J. Am. Chem. Soc. **139**, 4623 (2017).

[12] E. Sajadi, T. Palomaki, Z. Fei, W. Zhao, P. Bement, C. Olsen, S. Luescher, X. Xu, J. A. Folk, and D. H. Cobden, Gate-induced superconductivity in a monolayer topological insulator, Science **362**, 922 (2018).

[13] V. Fatemi, S. Wu, Y. Cao, L. Bretheau, Q. D. Gibson, K. Watanabe, T. Taniguchi, R. J. Cava, and P. Jarillo-Herrero, Electrically tunable low-density superconductivity in a monolayer topological insulator, Science **362**, 926 (2018).

[14] M. Kaiser, A. I. Baranov, and M. Ruck, Bi_2Pt($hP9$) by low-temperature reduction of $Bi_13Pt_3I_7$: Reinvestigation of the crystal structure and chemical bonding analysis, Z. Anorg. Allg. Chem. **640**, 2742 (2014).

[15] B. Wu, V. Barrena, H. Suderow, and I. Guillamón, Huge linear magnetoresistance due to open orbits in $\gamma-PtBi_2$, Phys. Rev. Res. **2**, 022042(R) (2020).

[16] L. Xing, R. Chapai, R. Nepal, and R. Jin, Topological behavior and Zeeman splitting in trigonal $PtBi_{2-x}$ single crystals, npj Quantum Mater. **5**, 10 (2020).

[17] Y. Feng, Q. Jiang, B. Feng, M. Yang, T. Xu, W. Liu, X. Yang, M. Arita, E. F. Schwier, K. Shimada, H. O. Jeschke, R. Thomale, Y. Shi, X. Wu, S. Xiao, S. Qiao, and S. He, Rashba-like spin splitting along three momentum directions in trigonal layered $PtBi_2$, Nat. Commun. **10**, 4765 (2019).

[18] G. Shipunov, I. Kovalchuk, B. R. Piening, V. Labracherie, A. Veyrat, D. Wolf, A. Lubk, S. Subakti, R. Giraud, J. Dufouleur, S. Shokri, F. Caglieris, C. Hess, D. V. Efremov, B. Büchner, and S. Aswartham, Polymorphic $PtBi_2$: Growth, structure, and superconducting properties, Phys. Rev. Mater. **4**, 124202 (2020).

[19] J. Wang, X. Chen, Y. Zhou, C. An, Y. Zhou, C. Gu, M. Tian, and Z. Yang, Pressure-induced superconductivity in trigonal layered $PtBi_2$ with triply degenerate point fermions, Phys. Rev. B **103**, 014507 (2021).

[20] W. Gao, X. Zhu, F. Zheng, M. Wu, J. Zhang, C. Xi, P. Zhang, Y. Zhang, N. Hao, W. Ning, and M. Tian, A possible candidate for triply degenerate point fermions in trigonal layered $PtBi_2$, Nat. Commun. **9**, 3249 (2018).

[21] K. Takaki, M. Yamamoto, M. Nakajima, T. Takeuchi, H. Y. Nguyen, M. Nohara, Y. Kishioji, T. Fujii, K. Yoshino, S. Miyasaka, and K. Kudo, Enhanced superconductivity in close proximity to polar-nonpolar structural phase transition in Se/Te-substituted $PtBi_2$, J. Phys. Soc. Jpn. **91**, 034703 (2022).

[22] L. Ji, M. S. Rzchowski, N. Anand, and M. Tinkham, Magnetic-field-dependent surface resistance and two-level critical-state model for granular superconductors, Phys. Rev. B **47**, 470 (1993).

[23] W. H. Tang, C. Y. Ng, C. Y. Yau, and J. Gao, Thickness dependence of superconductivity for $YBa_2Cu_3O_y$ ultra-thin films, Supercond. Sci. Technol. **13**, 580 (2000).

[24] Z. Wang, C. Liu, Y. Liu, and J. Wang, High-temperature superconductivity in one-unit-cell FeSe films, J. Phys.: Condens. Matter **29**, 153001 (2017).

[25] L. Bao, Y. Bi, X. Liu, X. Yang, T. Hao, S. Tian, Z. Wang, J. Li, and C. Gu, Thickness dependence of superconductivity in single-crystal $Ta_4Pd_3Te_{16}$ nanoribbons, Appl. Phys. Lett. **113**, 022603 (2018).

[26] J. Simonin, Surface term in the superconductive Ginzburg-Landau free energy: Application to thin films, Phys. Rev. B **33**, 7830 (1986).

[27] C. Yue, J. Hu, X. Liu, A. M. Sanchez, Z. Mao, and J. Wei, Nanoscale inhomogeneous superconductivity in $Fe(Te_{1-x}Se_x)$ probed by nanostructure transport, ACS Nano **10**, 429 (2016).

[28] C. dos Santos, M. da Luz, B. Ferreira, and A. Machado, On the transport properties in granular or weakly coupled superconductors, Physica C: Supercond. **391**, 345 (2003).

[29] S. V. Semenov, A. D. Balaev, and D. A. Balaev, Dissipation in granular high-temperature superconductors: New approach to describing the magnetoresistance hysteresis and the resistive transition in external magnetic fields, J. Appl. Phys. **125**, 033903 (2019).

[30] P. Muné, F. Fonseca, R. Muccillo, and R. Jardim, Magnetic hysteresis of the magnetoresistance and the critical current density in polycrystalline $YBa_2Cu_3O_{7-\delta}$–Ag superconductors, Physica C: Supercond. **390**, 363 (2003).

[31] D. A. Balaev, D. M. Gokhfeld, A. A. Dubrovskiĭ, S. I. Popkov, K. A. Shaikhutdinov, and M. I. Petrov, Magnetoresistance hysteresis in granular HTSCs as a manifestation of the magnetic flux trapped by superconducting grains in YBCO + CuO composites, J. Exp. Theor. Phys. **105**, 1174 (2007).

[32] I. Felner, E. Galstyan, B. Lorenz, D. Cao, Y. S. Wang, Y. Y. Xue, and C. W. Chu, Magnetoresistance hysteresis and critical current density in granular $RuSr_2Gd_{2-x}Ce_xCu_2O_{10-\delta}$, Phys. Rev. B **67**, 134506 (2003).

[33] H. Zhou and X. Jin, Stray field and vortex controlled magnetoresistance in superconducting Bi/Ni bilayers, J. Magn. Magn. Mater. **458**, 171 (2018).

[34] H. Ru, Y.-S. Lin, Y.-C. Chen, Y. Feng, and Y.-H. Wang, Observation of two-level critical state in the superconducting FeTe thin films, Chin. Phys. Lett. **36**, 077402 (2019).

[35] R. Sultana, P. Rani, A. K. Hafiz, Reena Goyal, and

V. P. S. Awana, An intercomparison of the upper critical fields (H_{c2}) of different superconductors—$YBa_2Cu_3O_7$, MgB_2, $NdFeAsO_{0.8}F_{0.2}$, $FeSe_{0.5}Te_{0.5}$ and Nb_2PdS_5, J. Supercond. Novel Magn. **29**, 1399 (2016).

[36] Z. Ye, H. Zhang, H. Liu, W. Wu, and Z. Luo, Observation of superconductivity in single crystalline Bi nanowires, Nanotechnology **19**, 085709 (2008).

[37] S. Schimmel, Y. Fasano, S. Hoffmann, J. Besproswanny, L. T. Corredor Bohorquez, J. Puig, B.-C. Elshalem, B. Kalisky, G. Shipunov, D. Baumann, S. Aswartham, B. Bchner, and C. Hess, Surface superconductivity in the topological Weyl semimetal t-$PtBi_2$, Nat. Commun. **15**, 9895 (2024).

[38] Y. Yuan, Y. Duan, Z. Wang, and J. Sun, Filamentary superconductivity in wrinkled $PtSe_2$, J. Phys. D **54**, 215302 (2021).